miniTRASGO: design and initial results of a compact Resistive Plate Chamber telescope for worldwide cosmic ray monitoring

C. Soneira-Landín*[1], A. Blanco[2], L. M. Fraile[1], J. A. Garzón[3], G. Kornakov[4], L. Lopes[2], J. Michel[5], V. M. Nouvilas[1], and J. M. Udías[1]

[1]Grupo de Física Nuclear, EMFTEL & IPARCOS, Universidad Complutense de Madrid, CEI Moncloa, 28040 Madrid, Spain
[2]Laboratório de Instrumentação e Física Experimental de Partículas (LIP), Rua Larga, Universidade de Coimbra, 3004-516 Coimbra, Portugal
[3]Laboratorio Carmen Fernández (LabCAF), Departamento de Física de Partículas, Universidade de Santiago de Compostela, Campus Vida, Rúa Xosé María Suárez Núñez, 15782 Santiago de Compostela, Spain
[4]Faculty of Physics, Warsaw University of Technology, Koszykowa 75, 00-662 Warsaw, Poland
[5]Institut für Kernphysik, Goethe-Universität, Max-von-Laue-Str. 1, 60438 Frankfurt, Germany

Abstract

Cosmic rays, composed primarily of high-energy protons and atomic nuclei, interact with Earth's atmosphere, generating secondary particles that can be detected at ground level. Understanding these interactions requires precise measurements across various geomagnetic and atmospheric conditions. To address this challenge, miniTRASGO is introduced: a cost-effective and portable cosmic ray detector based on Resistive Plate Chambers, designed for worldwide deployment. This study describes the miniTRASGO system, including its design, data acquisition, and calibration processes. The detector measures charged secondary cosmic rays, reconstructs particle trajectories, and accounts for environmental influences such as pressure and temperature. Performance evaluations indicate an angular precision better than 5° and an efficiency of approximately 95%. The first operational miniTRASGO stations, deployed in Madrid (Spain), Warsaw (Poland), Puebla, and Monterrey (Mexico), allow for multi-site monitoring of cosmic ray flux. A Forbush Decrease event observed in March 2024 by the Madrid station validates the detector's capability for space weather studies. The results highlight the potential of miniTRASGO to contribute to global cosmic ray monitoring, improving the characterization of cosmic ray variations and their implications for space weather.

Keywords: Cosmic rays; Solar-terrestrial relationship; Muon telescopes; Resistive Plate Chambers

1 Cosmic rays at Earth

Cosmic rays, primarily high-energy protons and atomic nuclei, reach Earth from beyond the Solar System. Their origin and the mechanisms capable of accelerating them to energies exceeding 10^{20} eV, far beyond current human technologies, remain unknown [Blasi, 2013]. Upon reaching Earth's atmosphere, cosmic rays undergo nuclear interactions that produce cascades consisting of secondary particles such as muons, electrons, gamma rays, and nucleons [Rossi, 1964]. These secondary components provide the basis for ground-based studies and play a crucial role in understanding the properties of primary cosmic rays and their interactions with atmospheric nuclei.

The study of cosmic rays is constrained by their energy-dependent flux. While cosmic rays above 10^{14} eV are rare and require indirect detection via air shower arrays [The Pierre Auger Collaboration, 2015], those in the range of 10^9 to 10^{14} eV are measured using satellite and balloon experiments that provide direct observations of their composition and energy spectra [Kampert and Watson, 2012]. At

*Corresponding author: csoneira@ucm.es; Tel: +34 638 726 960

lower energies, however, primary cosmic rays form a continuous flux that is shaped by Earth's magnetic field and modulated by solar activity. The geomagnetic field deflects low-rigidity particles, establishing a cutoff threshold that depends on latitude and altitude, while the solar wind modulates the flux of low-energy cosmic rays through interactions with the interplanetary magnetic field [Grieder, 2001]. These effects lead to temporal and spatial variations in cosmic ray intensity, which are essential for studying solar-terrestrial interactions.

1.1 Factors affecting cosmic ray flux at Earth

Atmospheric effects play a crucial role in the flux measured at ground, as secondary cosmic ray production occurs at varying depths in the atmosphere depending on particle type, and their survival probability is dictated by the amount of material they traverse [Dorman, 2004, Mendonça et al., 2019]. In regions where the geomagnetic rigidity cutoff is below 1 GV—such as near the poles—the threshold for secondaries is governed by atmospheric absorption. Under these conditions, calculations from Mishev and Poluianov [2021] show that the minimum proton energy required to reach the ground ranges from 428 MeV at sea level to 268 MeV at 4500 m, when considering atmospheric effects alone. At lower latitudes, however, the Earth's magnetic field imposes an additional rigidity cutoff, further restricting the range of cosmic rays that can penetrate the atmosphere. This results in latitude-dependent flux variations, as only particles above a certain rigidity can bypass the geomagnetic shielding and reach a given location.

A global network of detectors is essential to fully characterize these influences. Such measurements enable a comprehensive study of how atmospheric absorption and geomagnetic phenomena shape the observed cosmic ray spectrum, ensuring a more complete understanding of cosmic ray propagation and interactions across diverse environmental conditions.

1.2 Muons and Neutrons as Cosmic Ray Probes

At ground level, muons are the most abundant charged secondary component of cosmic rays. They originate primarily from the decay of pions and kaons at altitudes around 15-20 km. While muons eventually decay into electrons, their relativistic speeds extend their lifetime, allowing many to reach the Earth's surface. Due to their mass—approximately 206.8 times that of an electron—they experience minimal radiative losses, allowing them to penetrate up to several kilometers underground [Uretsky, 1997]. As a result, muons largely preserve their initial production angles and provide directional information, enabling angular analyses that offer insights into cosmic ray propagation and anisotropies.

Neutrons, a significant component of secondary cosmic radiation, are primarily produced via spallation reactions when cosmic rays interact with atmospheric nuclei [Grieder, 2001]. Once generated, neutrons may undergo further interactions within the atmosphere, decay within minutes, or reach the Earth's surface. Because neutrons originate from lower-energy primary cosmic rays compared to muons, they serve as effective probes of transient solar-terrestrial events. Simultaneous measurements of muons and neutrons thus provide complementary information, enabling better constraints on the properties of primary cosmic rays [Blanco et al., 2024].

1.3 Global cosmic ray monitoring: interest and current limitations

Ground-based networks have been established to monitor secondary cosmic rays. The Neutron Monitor Database (NMDB) provides long-term neutron flux measurements from detector designs such as NM64 and IGY, deployed in permanent stations [Steigies et al., 2008]. However, these detectors lack directional sensitivity, limiting their ability to detect cosmic ray anisotropies. The Global Muon Detector Network (GMDN), developed to measure cosmic ray variations using muon detectors, offers angular information but is constrained by the small number of operational stations, currently limited to four worldwide [Rockenbach et al., 2014].

Combining complementary instruments and pursuing global coverage enhances the study of cosmic rays, particularly during solar events that affect their propagation through the heliosphere [Blanco et al., 2024]. For example, Munakata et al. [2022] utilized both NMDB and GMDN to analyze the Forbush Decrease of November 2021—a sudden drop in cosmic ray intensity caused by the passage through Earth of interplanetary disturbances, such as coronal mass ejections (CMEs) and their associated shocks [Webb and Howard, 2012]. The study emphasized the potential of global cosmic ray monitoring to enhance the predictability of such events, which are crucial for space weather forecasting.

Beyond NMDB and GMDN, several distributed initiatives contribute continuous secondary-particle measurements suitable for space-weather studies. Among these networks, the Space Environment View-

ing and Analysis Network (SEVAN) deploys modular scintillator–lead stacks at middle and low latitudes, delivering real-time separation of neutron, muon, and electromagnetic components [Chilingarian et al., 2018]. The Latin American Giant Observatory (LAGO) operates autonomous water-Cherenkov detectors across a wide latitudinal range from Mexico to Antarctica, providing comprehensive flux data for Southern Hemisphere coverage [Sidelnik and Asorey, 2017]. Additionally, the Global Network of Cosmic Ray Detectors for Space and Terrestrial Weather Observation (gLOWCOST) project aims to establish a worldwide network of affordable muon detectors specifically designed for educational and research applications [Mubashir et al., 2025].

Complementing these dedicated networks, individual experiments contribute valuable data through secondary operational modes, including the Pierre Auger Observatory operating in scaler mode [The Pierre Auger Collaboration, 2025], and the Gamma Ray Astronomy at PeV Energies Phase-3 (GRAPES-3) experiment [Hariharan et al., 2023]. The persistence of limitations in scalability, operational costs, and geographic coverage among traditional monitoring networks highlights the strategic importance of these complementary detection systems, which collectively enhance global coverage while offering greater deployment flexibility and cost-effectiveness.

1.4 The TRASGO project: a scalable approach to cosmic ray detection

To address these limitations, the TRASGO (TRAck reconStructinG bOx) project was conceived as a versatile, scalable solution for cosmic ray detection using Resistive Plate Chambers (RPCs). While RPCs have been employed in cosmic ray studies [Aielli et al., 2006], the commissioning of the HADES RPC-TOF at GSI [Blanco et al., 2012] demonstrated their capabilities for detailed cosmic ray applications. These detectors present several advantages over traditional systems, such as neutron monitors and scintillator muon telescopes.

RPCs provide excellent timing resolution, reaching the order of hundreds of picoseconds [Xarepe et al., 2023], as well as excellent position resolution, intrinsically in the order of the millimeter. This gives good angular precision and leads to high granularity without the need to divide the active area, enabling the measurement of cosmic ray flux and arrival direction with much greater accuracy than conventional scintillator muon telescopes, which typically require segmentation of the active area and have lower timing resolution. This allows for precise tracking of individual cosmic ray events within a single compact station, whereas neutron monitors only provide integrated count rates without directional sensitivity. Beyond its performance benefits, the fundamental design of the RPCs developed at LIP [Saraiva and Blanco, 2024, Soneira-Landín et al., 2025] makes TRASGO a cost-effective and inherently scalable solution. This approach allows for straightforward replication and construction in various sizes without altering the core manufacturing methodology.

The TRASGO project extends these developments into a globally scalable framework for cosmic ray studies, providing a reliable tool for space weather monitoring and cosmic ray detection across diverse environments.

1.5 miniTRASGO: a new approach to cosmic ray flux monitoring

To facilitate broader accessibility and establish a distributed monitoring network, the miniTRASGO detector was developed as a portable, cost-effective adaptation of the TRASGO design [Soneira-Landín et al., 2025]. Maintaining the performance and compatibility of its larger counterparts, miniTRASGO is optimized for deployment across diverse locations, facilitating systematic studies of cosmic ray flux under varying conditions.

The first miniTRASGO has been operational at Universidad Complutense de Madrid (Spain) since September 2023, with additional stations established in Warsaw (Poland) and Puebla (Mexico) since the end of 2024, and Monterrey (Mexico) in early 2025. These locations cover a broad range of latitudes—Madrid (40°N), Warsaw (52°N), Puebla (19°N), and Monterrey (25°N)—with altitudes of 650 m, 78 m, 2150 m, and 540 m, respectively. Their corresponding magnetic cutoff rigidities are 7.2 GV, 2.8 GV, 7.5 GV, and 6.3 GV. The geographic diversity of the stations, spanning multiple latitudes, altitudes, and magnetic rigidities, provides valuable insights for a more comprehensive characterization of low-energy cosmic rays.

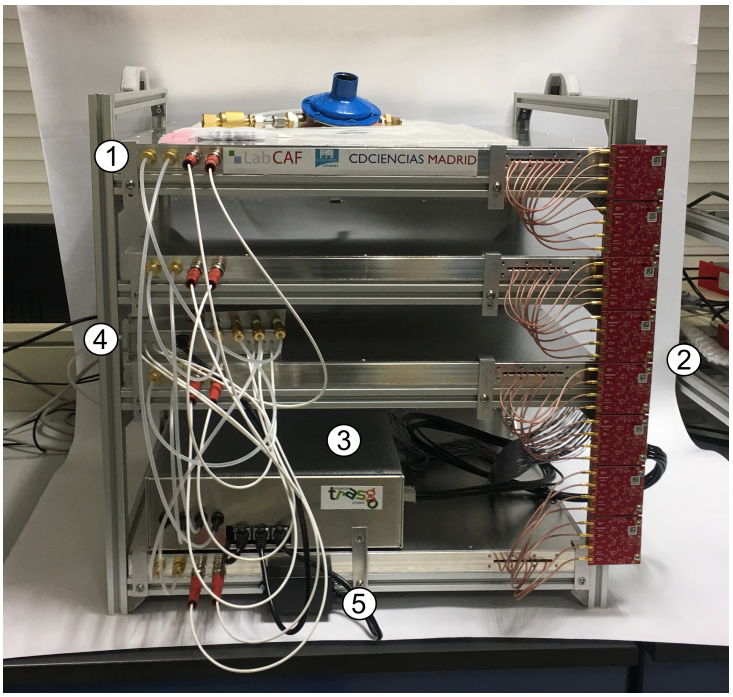

Figure 1: A miniTRASGO, fitting within a cubic volume of 50 cm per side. Key components visible in the setup include: (1) gas and high-voltage feedthroughs, (2) Front-End Electronics for signal processing, (3) a dedicated enclosure containing the data acquisition system and an embedded computer, (4) a compact, in-house high-voltage power supply, and (5) external environmental sensors.

2 The miniTRASGO system

MiniTRASGO is a detector for secondary charged cosmic rays, designed to measure the flux and direction of traversing particles. This is achieved through a reconstruction process that utilizes the timing and position of particle interactions recorded in the RPC planes.

The detector, shown in Fig. 1, consists of four multigap RPC modules [Zeballos et al., 1996], each encapsulated in a gas-tight plastic enclosure with feedthroughs for gas flow and high voltage (HV). The active area of each RPC module is 30×30 cm^2, and it is encased in an aluminum box for electromagnetic insulation and mechanical stability.

The modules are mounted in an aluminum frame with a maximum vertical span of 45 cm, allowing for easy adjustment of the spacing between planes. Currently, the planes are positioned equidistantly, with a separation of 15 cm; however, during part of the measurement campaign, the upper three planes were placed at equal intervals of 10 cm, while the lowest plane was positioned 20 cm below the third. The geometrical configuration can be adjusted as needed for specific applications, such as performing HV scans to determine the optimal operating point, where placing the planes in close proximity may be advantageous.

Every plane, see Fig. 2, has two gas gaps defined by three 2-mm-thick float glass electrodes (covering the active area), separated by 1-mm-diameter nylon monofilaments. The outermost glass surfaces are coated with a semi-conductive acrylic paint layer (10 MΩ/cm^2), applied by airbrushing to ensure uniform high-voltage distribution. For the Madrid detector, the operating voltage is typically fixed at approximately 5.5 kV per gap. Because the fundamental RPC operation parameter is the reduced electric field, E/n, expressed in Townsend units (Td), the working voltage depends on local pressure and temperature, which affect the neutral gas number density n. For this detector, the reduced field is $E/n \approx 220$ Td. Charged particles passing through the detector produce primary ionizations, releasing electrons. These primary electrons are accelerated by the electric field generated by the HV, leading to successive secondary ionizations. This process results in a Townsend avalanche, which induces a signal in the reading electrodes [Abbrescia et al., 2018].

The RPC plane is read out by a signal pickup electrode composed of four asymmetric copper strips positioned on the top surface of the RPC plastic box: one strip, referred to as the *wide strip*, measuring 98 mm in width, and three strips, referred to as the *narrow strips*, each 63 mm wide. This layout is

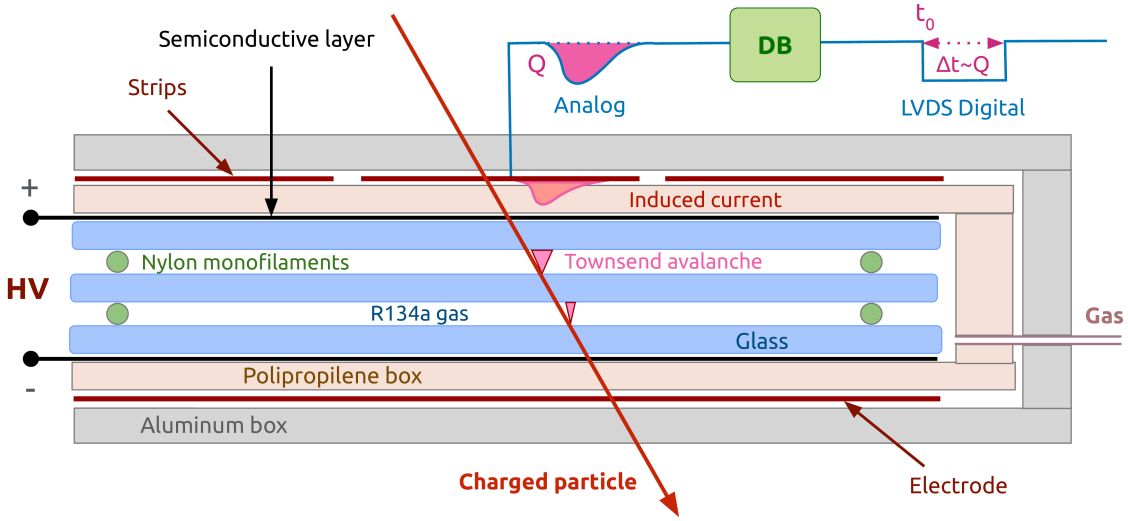

Figure 2: Two-gap RPC configuration enclosed in a polypropylene box with external readout strips (not to scale). Charged particles ionize the detector gas, and the resulting electrons, accelerated by the electric field, trigger a Townsend avalanche, inducing a signal in the readout electrodes. The Front-End Electronics converts the signal into a Low Voltage Differential Signal.

illustrated in Fig. 3. Each strip has a length of 300 mm. The readout system is complemented by a planar, unsegmented copper electrode positioned at the bottom surface of the RPC plastic box, which acts as a reference plane and enhances signal transmission acting as a waveguide for the induced signal along the strips. The strips are read at the Front (F) and Back (B) ends along the longitudinal direction. The asymmetric geometry allows for improved trajectory reconstruction while reducing the number of required readout channels. Angular reconstruction uncertainty is discussed in Subsec. 4.1.

Signals are processed by high-speed Front-End Electronics (FEE) based on the HADES Time-of-Flight Wall FEE [Belver et al., 2010], achieving a time jitter below $\sigma = 30$ ps and capable of providing an estimation of charge via Time-over-Threshold (ToT) method with an integration time of 100 ns. Processed signals are sent to a TRB3sc [Neiser et al., 2013], a 32-channel Time-to-Digital Converter (TDC) with a time jitter below $\sigma = 20$ ps that serves as both the data acquisition system (DAQ) and the trigger logic unit.

The telescope operates in an open, monitored, gas loop of R134a and it measures environmental conditions via integrated sensors for temperature, humidity and pressure. The schematics of the system are shown in Fig. 4. Real-time data analysis and monitoring are automated and accessible remotely via a Telegram bot and Grafana [Grafana Labs, 2025].

3 Data acquisition, processing and calibration

Charged particles entering the detector may produce a Townsend avalanche which leads to the propagation of a signal. This signal is processed by the FEE and transmitted to the TDC as a Low Voltage Differential Signal (LVDS) when it exceeds the discriminator threshold. Signals are recorded if they reach the TDC from at least two consecutive planes or the non-consecutive planes 1 and 3, within a 50 ns time window. The DAQ also allows for stricter 3- or 4-plane triggers, as well as a single-plane trigger mode, in which every signal reaching the TRB3sc is acquired.

The signal from the FEE encodes timing information on the leading edge, while charge information is carried on the trailing edge and is effectively determined by subtracting the two edge times. These variables enable the estimation of the particle position and time of incidence, allowing for trajectory reconstruction.

3.1 Charge produced by the avalanche

In RPCs, the charge produced in an avalanche does not consistently scale with the energy of the incident particle [Fonte et al., 2000]. Detectable variations beyond the typical stochastic fluctuations of the

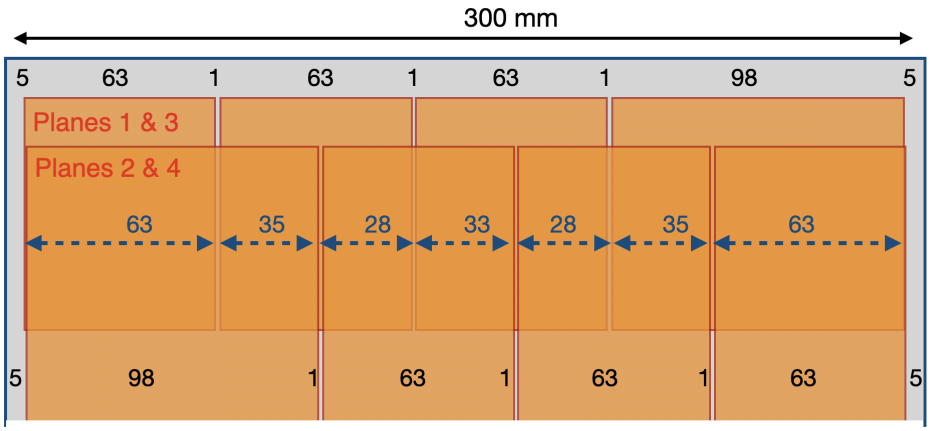

Figure 3: Geometry of the signal pickup electrodes, designed to enhance trajectory reconstruction. All numbers denote dimension in mm. Note the alternating pattern of wide and narrow strips.

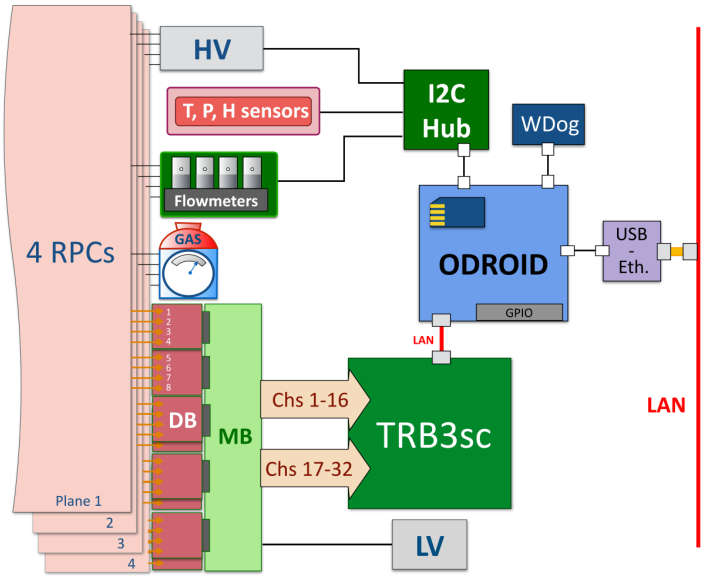

Figure 4: Complete schematic of the miniTRASGO system, including data acquisition, slow control, and environmental monitoring subsystems. The Resistive Plate Chambers (RPCs) receive high voltage (HV) from a dedicated power supply. The signals generated in the RPCs are processed by the Front-End Electronics (FEE), consisting of Daughterboards (DB) and a Motherboard (MB), which are fed by a low-voltage (LV) power supply. The processed signals are then sent to the Time Readout Board (TRB3sc). An ODROID computer reads the TRB3sc data and manages slow control via an I2C Hub, which monitors the flowmeters, environmental sensors (temperature, pressure, and humidity), and controls the HV settings. A watchdog (WDog) system ensures reliable operation by monitoring the ODROID status and triggering a reset if necessary. The system is connected to a local network (LAN) for data transmission and remote access.

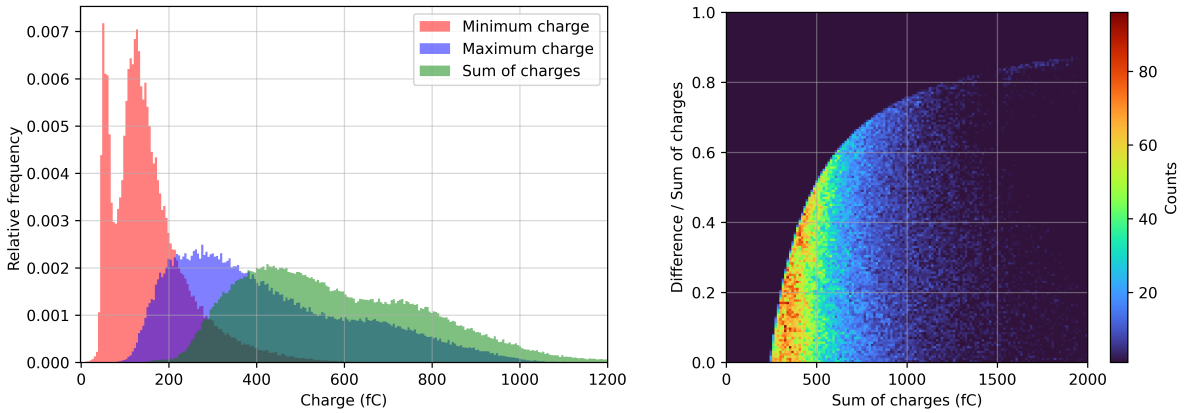

Figure 5: Left: Charge spectra for double hits. The left peak in the minimum charge distribution corresponds to crosstalk, while the right peak corresponds to charge collected in both adjacent strips. Right: Shared charge asymmetry (difference over sum) versus total charge sum for adjacent double hits after crosstalk removal.

charge generated by a single particle require the simultaneous passage of tens of particles. This inherent variability makes it impossible to measure the energy of the incident particles or reliably determine whether one or multiple particles interacted within a region of the RPC. Therefore, the collected charge is used for monitoring and for determining the position along the direction perpendicular to the strips. The charge in a strip is calculated as in Eq. 1,

$$Q_{P,s} = \frac{(Q^F_{P,s} + \varepsilon^{Q,F}_{P,s}) + (Q^B_{P,s} + \varepsilon^{Q,B}_{P,s})}{2}, \tag{1}$$

where $\varepsilon^{Q,F}_{P,s}$ and $\varepsilon^{Q,B}_{P,s}$ are offset parameters for the Front and Back sides of strip s in plane P. The total charge of each plane, Q_P, is given by the sum of the charges collected across all its strips.

Ionizations inside the gas gap could develop into streamers—large, saturated avalanches that increase dead time and compromise the aging of the RPCs. The detector operates exclusively with pure R134a, which is prone to streamer formation and requires close monitoring of its fraction [Abbrescia et al., 2018]. However, this approach eliminates the need for gas mixing systems, simplifying deployment by requiring only a direct connection to the gas bottle.

3.1.1 Crosstalk and interstrip characterization

Each RPC plane detects signals, according to the number of strips fired, as single ($n = 1$), double ($n = 2$), triple ($n = 3$), or quadruple ($n = 4$) hits, collectively termed *cluster size* [Abbrescia et al., 2018]. Multi-strip detections ($n \geq 2$) may result from multiple particles, charge sharing, or crosstalk, where capacitive coupling falsely increases n.

For $n = 2$, if the strips are adjacent, the charge spectrum for the strip collecting minimum value exhibits a bimodal distribution, see Fig. 5, left. The left peak corresponds to crosstalk, while the right peak represents charge shared between strips, defining events categorized as interstrip. The asymmetry of the charge collected in adjacent strips, defined as the difference over the sum, exhibits a relationship with the total charge sum for adjacent double hits after crosstalk removal, see Fig. 5, right. This relationship could be used for monitoring purposes, to study multiplicities of particles inside of the detector or to improve the position resolution.

3.2 Position in the direction perpendicular to the strips

The Y position is defined along the axis perpendicular to the strips. Once the charge for every strip in an RPC has been calculated, the Y position is determined according to the strips fired: the detection is set in a random uniform position in the width of the strip that collected the largest charge. The algorithm is improved accounting for interstrip cases as those that happen in the middle of two strips, according to the charge asymmetry value (Fig. 5, right). Uniform distribution on the strips widths gives uncertainties of $\sigma(Y_{\text{narrow}}) = 63/\sqrt{12}$ mm $= 1.8$ cm and $\sigma(Y_{\text{wide}}) = 98/\sqrt{12}$ mm $= 2.8$ cm, where the factor $\sqrt{12}$ accounts

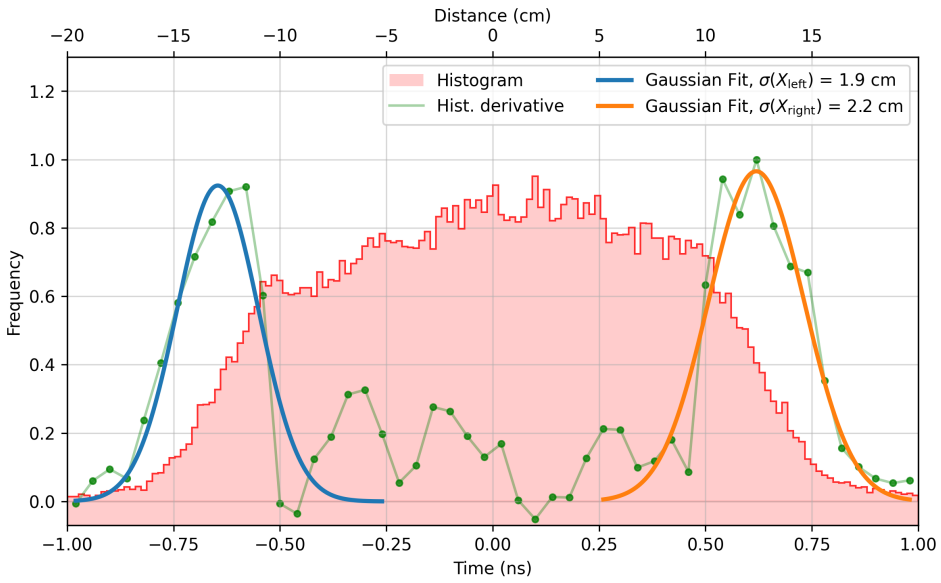

Figure 6: Position uncertainty estimation using the derivative method. The red histogram represents the T_{diff} distribution, while the green points correspond to its derivative in absolute value. The blue and orange curves represent Gaussian fits to the derivative peaks, with their respective standard deviations (σ) providing a measure of position uncertainty.

for the standard deviation of a uniform distribution over a given interval, as is commonly practiced in such calculations [Sehgal et al., 2020].

3.3 Position along the strip

The X position is defined along the axis parallel to the strips. The longitudinal position along the strip s in plane P, $X_{P,s}$, is obtained from the time difference between the Front (F) and Back (B) sides of the strip, with $\varepsilon^{X}_{P,s}$ as the offset parameter accounting for cable length, where V_{strip} is the signal propagation speed along the strip. See Eq. 2.

$$X_{P,s} = \frac{T^{F}_{P,s} - T^{B}_{P,s}}{2} \cdot V_{\text{strip}} + \varepsilon^{X}_{P,s}, \;\; \sigma\left(X\right) \approx 2 \text{ cm}. \tag{2}$$

Uncertainty is estimated from the width of a Gaussian fit to the derivative of the position histogram edges. Ideally, sharp histogram edges would produce a Dirac delta function in its derivative. In practice, deviations from this ideal case result in a broader distribution, which is approximated by a Gaussian. The width of this Gaussian quantifies the position uncertainty [Cortesi et al., 2007]. See Fig. 6.

3.4 Time of incidence

The time of incidence of the particle measured in the plane P and strip s, $T^{0}_{P,s}$, is calculated by averaging the times from the Front and Back sides of a strip, correcting for the signal propagation time along its length, L, and adding a calibration scalar to account for cable length, $\varepsilon^{T^0}_{P,s}$, see Eq. 3.

$$T^{0}_{P,s} = \frac{T^{F}_{P,s} + T^{B}_{P,s} - L/V_{\text{strip}}}{2} + \varepsilon^{T^0}_{P,s}, \;\; \sigma\left(T^{0}\right) \approx 300 \text{ ps}. \tag{3}$$

The time assigned to signals in each TRB3sc channel, which requires offset calibration, has a precision of hundreds of ps, dominated by the RPC. This offset calibration is performed using a software tool designed by the authors for this purpose that also calculates timing uncertainty. The software: (1) computes time differences for particle paths assuming the speed of light, (2) calculates offsets between detection differences, (3) derives an average offset matrix (4×4) by treating the set of strips as a network and considering all paths connecting them. The resulting offset matrix contains 16 values of $\varepsilon^{T^0}_{P,s}$, with $\varepsilon^{T^0}_{1,1} = 0$, as all times are referenced to strip 1 in plane 1.

4 Evaluation of the detector performance

4.1 Angular reconstruction uncertainty analysis

To assess the uncertainty in angular reconstruction, a Monte Carlo simulation was performed using a custom Python-based tool that generates cosmic muons according to well-established models. The surface muon intensity depends on both momentum and zenith angle. Empirical studies indicate that for low momenta ($p_\mu \approx 3$ GeV), the angular distribution follows a $\cos^n(\theta)$ dependence with $n \approx 2$, while at higher momenta ($p_\mu > 100$–200 GeV), it transitions towards a secant dependence ($\sec\theta$) within approximately $\theta < 70°$; at larger zenith angles the rapidly increasing slant depth of atmosphere suppresses the flux exponentially, so the total rate remains vertically dominated [Grieder, 2001]. To provide a unified description across all angles, Reyna [2006] introduced a simplified parameterization given by Eq. 4:

$$I(p_\mu, \theta) = \cos^3(\theta) I_V(p_\mu \cos\theta), \tag{4}$$

where $I_V(p_\mu)$ represents the vertical intensity, initially parameterized by Bugaev et al. [1998] and later refined by Reyna [2006] as expressed in Eq. 5:

$$I_V(p_\mu) = c_1 p_\mu^{-1\left(c_2 + c_3 \log_{10}(p_\mu) + c_4 \log_{10}^2(p_\mu) + c_5 \log_{10}^3(p_\mu)\right)}. \tag{5}$$

The parameter values employed in the simulation are presented in Eq. 6:

$$\begin{aligned} c_1 &= 0.00253, \\ c_2 &= 0.2455, \\ c_3 &= 1.288, \\ c_4 &= -0.2555, \\ c_5 &= 0.0209. \end{aligned} \tag{6}$$

Multiple scattering effects were estimated using Molière formula [Lynch and Dahl, 1991], which describes the standard deviation of the scattering angle, as given in Eq. 7. Here, c is the speed of light, $\beta = v/c$ is the particle velocity relative to c, v is the particle velocity, p its momentum, L_0 the thickness of the traversed material, and X_0 its radiation length.

$$\theta_0 = \frac{13.6 \text{ MeV}}{\beta c p} \sqrt{\frac{L_0}{X_0}} \left\{ 1 + 0.038 \ln\left(\frac{L_0}{X_0}\right) \right\}. \tag{7}$$

Fig. 7 illustrates the relationship between muon energy, incident angle, and scattering angle after traversing the detector. To enhance visualization, only five representative incident angles are displayed. Based on these simulations, straight trajectories—defined as those minimally affected by multiple scattering—correspond to muons with energies above approximately 1 GeV, given the material budget of the miniTRASGO.

Finally, a simulation for straight trajectories was conducted to determine angular uncertainty. The results indicate that, in the equidistant plane setup, the relative angular uncertainty remains below 3% in both the zenith (spanning 180°) and azimuth (spanning 360°) directions, as shown in Fig. 8.

4.2 Charge measurement

An avalanche within the gas gap induces a signal in one or more strips. The charge spectra for different cluster sizes of strips are displayed in Fig. 9, left. Single-strip detections dominate the spectrum, while events involving multiple strips exhibit a broader charge distribution. The distribution of the number of strips in each event and RPC plane is shown in Fig. 9, right. Single hits dominate ($\approx 90\%$), double detections account for $\approx 10\%$, while detections involving more strips are significantly rarer. Larger cluster sizes tend to appear on the lower planes, possibly due to electron-initiated showers within the detector. While this effect warrants further study to fully understand its origin, it represents a very small fraction of the data, does not significantly impact the overall performance of the telescope, and can be effectively filtered out if needed.

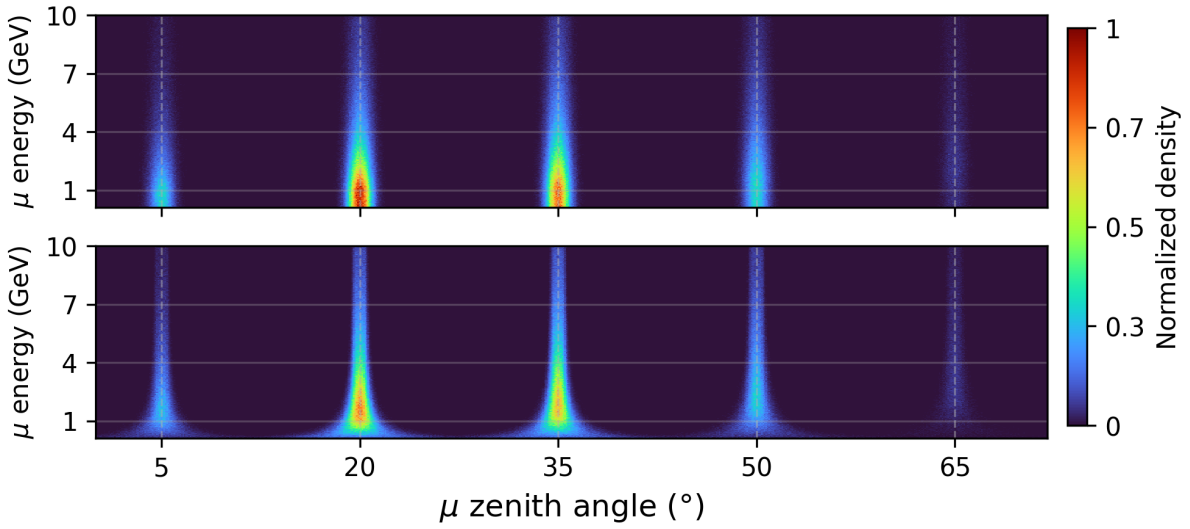

Figure 7: Simulated muon energy distributions as a function of their incident (top panel) and final scattering zenith angles (bottom panel) after traversing the detector. The color scale represents the density of simulated events, and for clarity, only five representative incoming zenith angles are shown. These results indicate that muons with energies above approximately 1 GeV (top panel) undergo only minimal deflection in the detector (bottom panel), producing effectively straight trajectories. Conversely, lower-energy muons exhibit greater multiple scattering, consistent with the material budget of the telescope.

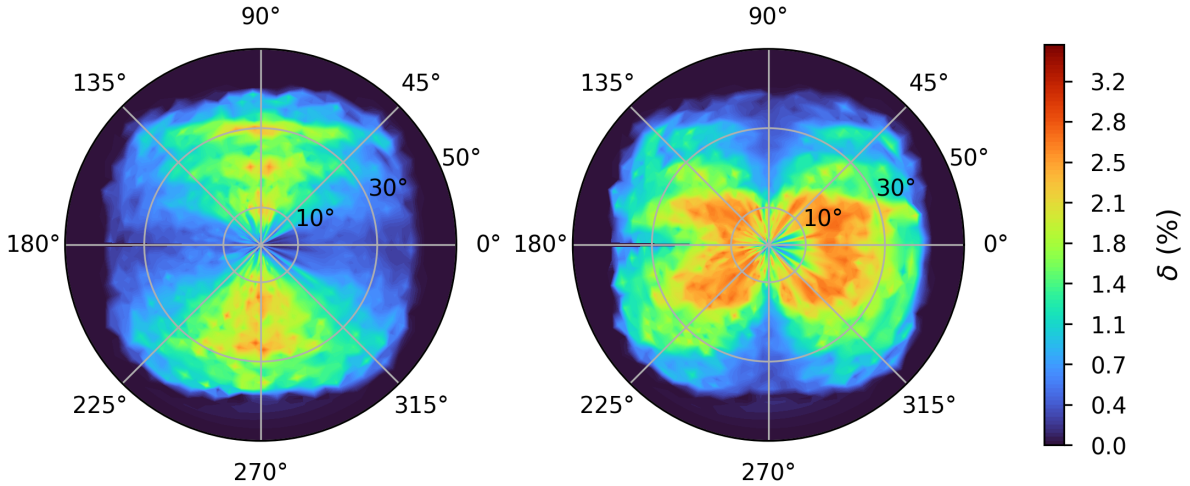

Figure 8: Polar binned density plots illustrating the relative angular uncertainties obtained from Monte Carlo simulations for straight trajectories detected across four equidistant planes. In these plots, the radial coordinate represents the zenith angle, while the angular coordinate corresponds to the azimuth angle, such that each point in the polar diagram denotes an incident trajectory on the celestial sphere. The left panel depicts the relative uncertainty in the zenith angle (spanning 180°), while the right panel shows the relative uncertainty in the azimuth angle (spanning 360°), both remaining below a maximum of 3%.

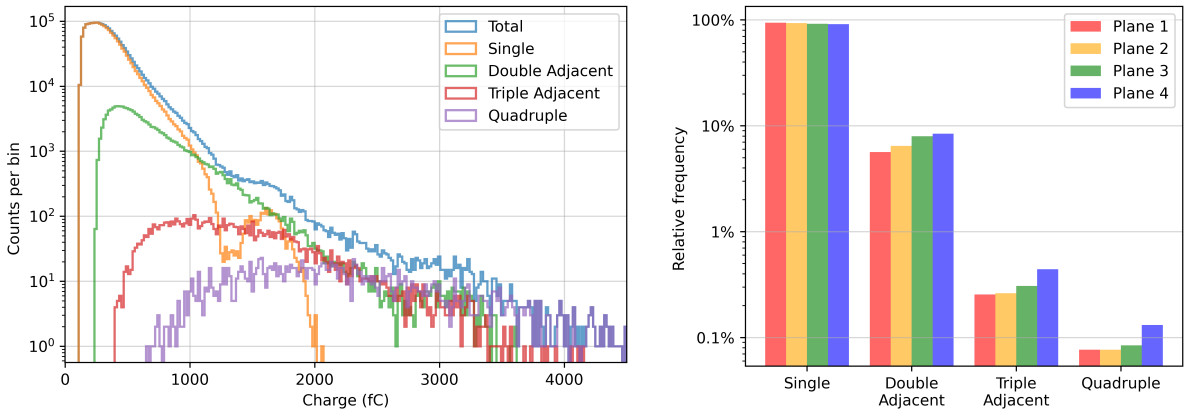

Figure 9: Left. Total charge spectrum per detection, categorized by the number of strips with signal above the crosstalk threshold. The different curves represent events detected in single strips, as well as in multiple adjacent strips (double, triple, and quadruple detections). The charge distribution for single-strip detections dominates, while multi-strip detections contribute at higher charge values. Note the streamer region in the single strip case between $1500 - 2000$ fC. Right. Relative frequency of n-strip detections per event. Multi-strip detections are more frequent in the lower planes, possibly due to electron-initiated showers. This effect is minimal and does not impact the telescope's overall performance.

4.3 Efficiency

Environmental conditions, particularly pressure and temperature, affect the detector gain, making corrections necessary for accurate measurement of arriving particle rates. Efficiency corrections help compensate for these variations.

MiniTRASGO allows for efficiency calculation using its four detection planes without relying on additional reference detectors. The efficiency of a given RPC plane is determined by analyzing particle tracks. A trajectory is classified as crossing if it is identified by signals in the other three RPCs and the reconstruction indicates that the particle should have traversed the plane of interest. If the plane also registers a detection, the event is classified as detected. The efficiency is then calculated as the ratio of detected to crossing events. The measured efficiency for each individual RPC is approximately 95%.

5 Secondary Cosmic ray rates

5.1 Counting rates and atmospheric corrections

5.2 Counting rates and atmospheric corrections

Considering the active area of 30×30 cm^2 and its geometric acceptance, the expected integrated count rate at sea level, based on the standard muon flux of approximately 70 m^{-2}s^{-1}sr^{-1}, is on the order of 70000 counts per hour [Grieder, 2001]. This count rate yields a statistical accuracy of approximately 0.4% for hourly measurements. While this precision is lower than that of large, traditional detectors such as neutron monitors, which benefit from much larger surface areas, it is important to note that this level of statistical accuracy is well-suited for the primary objectives of the miniTRASGO network. Solar transient events, such as Forbush decreases or ground-level enhancements, typically produce cosmic ray intensity variations of several percent and persist for multiple hours to days, making them easily detectable above the 0.4% hourly statistical noise floor. Furthermore, for longer-term studies or weaker signals, the statistical precision can be enhanced through temporal binning over multiple hours or days. The miniTRASGO detector prioritizes portability, cost-effectiveness, and ease of deployment while maintaining sufficient sensitivity for space weather monitoring and cosmic ray anisotropy studies.

Filtering out noise of the raw rate yields the processed rate, achieved through software that calibrates positions and charges, verifies coincidence windows, valid positions within RPCs, non-crosstalk charge values, and other criteria. A fitting algorithm developed by the authors, TimTrack [Garzón and Cabanelas, 2012], further cleans spurious detections.

Atmospheric pressure significantly influences the observed secondary cosmic ray rate, and correcting for it provides a more accurate measurement of the primary cosmic ray flux variations in the upper

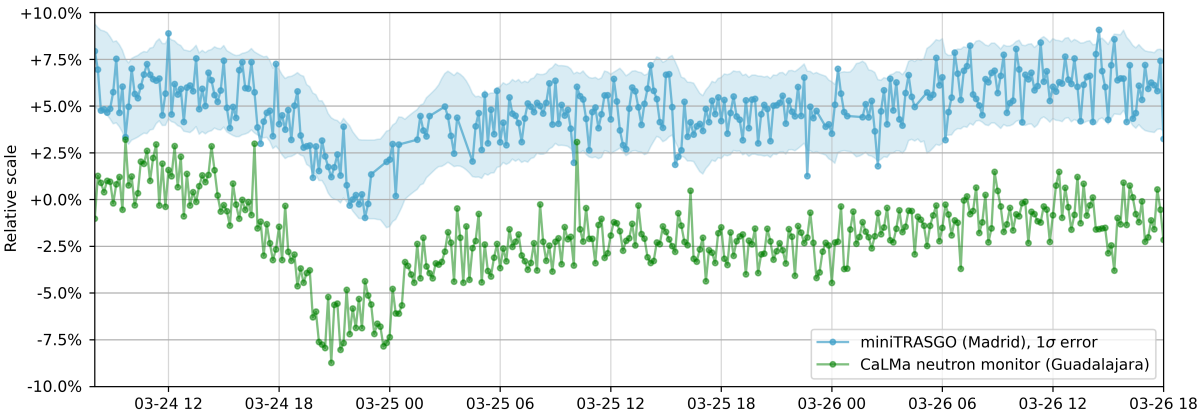

Figure 10: Efficiency- and pressure-corrected cosmic ray rates from miniTRASGO and CaLMa neutron monitor, showing the Forbush Decrease detected by both stations between March 24 and 25, 2024.

atmosphere. In accordance with standard practice [Maghrabi and Almutairi, 2018], the observed rate I is fitted as a function of pressure P using the barometric coefficient η_P. In this formulation, I_0 represents the mean rate over a given period (around two months), P_0 is the mean pressure, and ΔP is the difference between the instantaneous pressure P and P_0. The parameter η_P is determined by fitting the linear relationship between the logarithm of the normalized intensity, $\ln(I/I_0)$, and ΔP. The corrected rate I_{corr} is then calculated as in Eq. 8, where I_{meas} is the measured rate before correction. For the miniTRASGO in Madrid during the observations reported in the present study, $\eta_P = -0.215 \pm 0.038$ %/mbar.

$$\ln\left(\frac{I}{I_0}\right) \cdot 100\% = -\eta_P \cdot (P - P_0) \implies$$
$$I_{\text{corr}} = I_{\text{meas}} \cdot \exp\left(\frac{-\eta_P}{100\%} \cdot \Delta P\right) \tag{8}$$

5.3 Forbush Decrease Detection

A Forbush Decrease is a transient reduction in cosmic ray intensity, primarily driven by interplanetary magnetic field disturbances linked to solar activity [Forbush, 1937, 1938]. These events are crucial for understanding the interaction between the solar wind and Earth's magnetosphere.

Between March 24 and 25, 2024, a Forbush Decrease was observed by the miniTRASGO detector in Madrid, Spain (40.4°N, 3.7°W, 650 m), where the vertical cutoff rigidity is $R_c = 7.2$ GV [Gerontidou et al., 2021, Belov et al., 2021]. This was the first and only miniTRASGO deployed at that time. The event was observed in cosmic ray rate data, corrected for efficiency and pressure, showing an approximate 5% decrease from the baseline intensity in the miniTRASGO, as shown in Fig. 10. This observation aligns with data from the NMDB [Steigies et al., 2008], particularly when compared to the nearby CaLMa neutron monitor, which recorded a 7.5% decrease. The observed difference in the decrease is consistent with the higher rigidity cutoff of muons relative to neutrons, as discussed in Subsec. 1.2 and utilized in Blanco et al. [2024]. Consequently, the Forbush Decrease appears more pronounced in neutron monitors, highlighting the complementary role of muon and neutron measurements in cosmic ray studies.

The CaLMa cosmic ray detector, located in Guadalajara, Spain (40.63°N, 3.2°W, 708 m), is situated 53 km from miniTRASGO, and the altitude difference between the two sites is 42 m, which does not introduce significant discrepancies for direct comparisons.

This preliminary detection highlights the capability of the miniTRASGO detector to perform stable measurements of transient cosmic ray events, demonstrating its potential for space weather studies.

6 Conclusions and outlook

The miniTRASGO detector offers a compact, cost-effective solution for ground-based cosmic ray monitoring. Based on Resistive Plate Chambers, it achieves an angular precision better than 5° and an efficiency of approximately 95% under varying atmospheric conditions. The successful detection of a

Forbush Decrease in March 2024 at the Madrid station demonstrates its capability to detect transient cosmic ray variations.

Looking ahead, future work will focus on fully exploiting the detector trajectory reconstruction to refine atmospheric corrections and study directional cosmic ray rates. In parallel, the initiation of coordinated measurements across the miniTRASGO network, along with its expansion, will enable multi-site observations, providing a more comprehensive characterization of cosmic ray fluxes and enhancing space weather studies.

Acknowledgments

We acknowledge the NMDB database (https://www.nmdb.eu), founded under the European Union's FP7 programme (contract no. 213007) for providing data. CaLMa neutron monitor data were kindly provided by the Space Research Group (SRG-UAH), University of Alcalá, Spain.

This work was funded in part by the Spanish MCIN/AEI/10.13039/501100011033 under grant PID2021-126998OB-I00, by the Grupo de Física Nuclear (910059) at Universidad Complutense de Madrid, and by the project CPP2021-008751 "Nueva Generación de Dispositivos de Imagen Molecular en Mama (NeWMBI)", funded by the Ministerio de Ciencia e Innovación under the "Proyectos I+D+i en colaboración público-privada 2021" program. Additional support was provided by the Xunta de Galicia through grant ED431B 2021/012 as part of the "Consolidation of Competitive Research Units" program and by the Comunidad de Madrid through project PR47/21 (PRTR) TAU-CM.

This work utilizes the TRB3sc, part of the Data Acquisition System developed by the HADES collaboration at GSI. We acknowledge their design and appreciate their responsiveness and assistance in addressing our inquiries.

The authors thank P. Cabrales, P. Galve and J. J. Blanco for their assistance with proofreading and helpful suggestions to improve the clarity of the manuscript.

References

M. Abbrescia, V. Peskov, and P. Fonte. *Basics of Resistive Plate Chambers*, chapter 3, pages 45–110. John Wiley & Sons, Ltd, 2018. ISBN 9783527698691. doi: doi:https://doi.org/10.1002/9783527698691.ch3.

G. Aielli, R. Assiro, C. Bacci, B. Bartoli, P. Bernardini, X.J. Bi, B. Biondo, C. Bleve, S. Bricola, F. Budano, S. Bussino, A.K. Calabrese Melcarne, P. Camarri, D. Campana, Z. Cao, R. Cardarelli, S. Catalanotti, S. Cavaliere, M. Cavalli Sforza, P. Celio, N. Cheng, P. Creti, G. Cusumano, B.Z. Dai, G. D'Alí Staiti, Danzengluobu, B. D'Aquino, E. De Marinis, I. De Mitri, B. D'Ettorre Piazzoli, M. De Vincenzi, T. Di Girolamo, X.H. Ding, G. Di Sciascio, C.F. Feng, Zhaoyang Feng, Zhenyong Feng, K. Fratini, X.F. Gao, Q.B. Gou, H.H. He, M. He, Haibing Hu, Hongbo Hu, Q. Huang, M. Iacovacci, I. James, H.Y. Jia, Labaciren, H.J. Li, J.Y. Li, B. Liberti, G. Liguori, C.Q. Liu, J. Liu, H. Lu, G. Mancarella, A. Mangano, S.M. Mari, G. Marsella, D. Martello, S. Mastroianni, X.R. Meng, J. Mu, L. Nicastro, C.C. Ning, M. Panareo, G. Pellizzoni, L. Perrone, C. Pino, C. Pinto, P. Pistilli, E. Reali, E. Rossi, L. Saggese, P. Salvini, R. Santonico, P.R. Shen, X.D. Sheng, F. Shi, C. Stanescu, A. Surdo, Y.H. Tan, P. Vallania, S. Vernetto, H. Wang, Yonggang Wang, Yungang Wang, C.Y. Wu, H.R. Wu, L. Xue, H.T. Yang, Q.Y. Yang, X.C. Yang, G.C. Yu, A.F. Yuan, M. Zha, H.M. Zhang, J.L. Zhang, L. Zhang, N.J. Zhang, P. Zhang, X.Y. Zhang, Y. Zhang, Zhaxisangzhu, X.X. Zhou, F.R. Zhu, and Q.Q. Zhu. Layout and performance of RPCs used in the Argo-YBJ experiment. *Nuclear Instruments and Methods in Physics Research Section A: Accelerators, Spectrometers, Detectors and Associated Equipment*, 562(1):92–96, 2006. ISSN 0168-9002. doi: https://doi.org/10.1016/j.nima.2006.02.136.

S. M. Belov, E. Zobnin, and V. G. Yanke. Cutoff rigidity and particle trajectories online calculator. *NMDB@Home 2020: Proceedings of the 1st virtual symposium on cosmic ray studies with neutron detectors*, 1:197–203, 2021. ISSN 2748-3150. doi: 10.38072/2748-3150/p24.

D. Belver, P. Cabanelas, E. Castro, J. A. Garzón, A. Gil, D. Gonzalez-Diaz, W. Koenig, and M. Traxler. Performance of the Low-Jitter High-Gain Bandwidth Front-End Electronics of the HADES tRPC Wall. *IEEE Transactions on Nuclear Science*, 57(5):2848–2856, 2010. doi: 10.1109/TNS.2010.2056928.

A. Blanco, D. Belver, P. Cabanelas, J. Díaz, P. Fonte, J.A. Garzón, A. Gil, D. Gonzalez-Díaz, W. Koenig, B. Kolb, L. Lopes, M. Palka, A. Pereira, M. Traxler, and P. Zumbruch. RPC HADES-TOF wall cosmic ray test performance. *Nuclear Instruments and Methods in Physics Research Section A: Accelera-*

tors, Spectrometers, Detectors and Associated Equipment, 661:S114–S117, 2012. ISSN 0168-9002. doi: https://doi.org/10.1016/j.nima.2010.08.068. X. Workshop on Resistive Plate Chambers and Related Detectors (RPC 2010).

J. J. Blanco, S. Ayuso, A. Regadío, A. López-Comazzi, J. I. García-Tejedor, Ó. García-Población, and C. L. Guerrero Contreras. Evolution of the cosmic ray spectrum during a Forbush decrease. *Advances in Space Research*, 73(9):4842–4852, 2024. ISSN 0273-1177. doi: https://doi.org/10.1016/j.asr.2024.02.026.

P. Blasi. The origin of galactic cosmic rays. *Astronomy and Astrophysics Review*, 21(1):70, 2013. doi: 10.1007/s00159-013-0070-7.

E. V. Bugaev, A. Misaki, V. A. Naumov, T. S. Sinegovskaya, S. I. Sinegovsky, and N. Takahashi. Atmospheric muon flux at sea level, underground, and underwater. *Phys. Rev. D*, 58:054001, Jul 1998. doi: 10.1103/PhysRevD.58.054001.

A. Chilingarian, V. Babayan, T. Karapetyan, B. Mailyan, B. Sargsyan, and M. Zazyan. The SEVAN Worldwide network of particle detectors: 10 years of operation. *Advances in Space Research*, 61 (10):2680–2696, 2018. ISSN 0273-1177. doi: https://doi.org/10.1016/j.asr.2018.02.030. URL `https://www.sciencedirect.com/science/article/pii/S0273117718301728`.

M. Cortesi, R. Alon, R. Chechik, A. Breskin, D. Vartsky, and V. Dangendorf. Investigations of a THGEM-based imaging detector. *Journal of Instrumentation*, 2:P09002, September 2007. doi: 10.1088/1748-0221/2/09/P09002.

L. Dorman. *Cosmic Rays in the Earth's Atmosphere and Underground*, volume 303 of *Astrophysics and Space Science Library*. Kluwer Academic Publishers, Dordrecht, 2004. doi: 10.1007/1-4020-2071-6.

P. Fonte, A. Smirnitski, and M.C.S. Williams. A new high-resolution TOF technology. *Nuclear Instruments and Methods in Physics Research Section A: Accelerators, Spectrometers, Detectors and Associated Equipment*, 443(1):201–204, 2000. doi: 10.1016/S0168-9002(99)01008-6.

S. E. Forbush. On the effects in cosmic-ray intensity observed during the recent magnetic storm. *Physical Review*, 51(12):1108–1109, 1937. doi: 10.1103/PhysRev.51.1108.3.

S. E. Forbush. On world-wide changes in cosmic-ray intensity. *Physical Review*, 54(12):975–988, 1938. doi: 10.1103/PhysRev.54.975.

J. A. Garzón and P. Cabanelas. TimTrack: A matrix formalism for a fast time and track reconstruction with timing detectors. *Nuclear Instruments and Methods in Physics Research Section A: Accelerators, Spectrometers, Detectors and Associated Equipment*, 661:S210–S213, 2012. ISSN 0168-9002. doi: 10.1016/j.nima.2010.09.170. X. Workshop on Resistive Plate Chambers and Related Detectors (RPC 2010).

M. Gerontidou, N. Katzourakis, H. Mavromichalaki, V. Yanke, and E. Eroshenko. World grid of cosmic ray vertical cut-off rigidity for the last decade. *Advances in Space Research*, 67(7):2231–2240, 2021. ISSN 0273-1177. doi: https://doi.org/10.1016/j.asr.2021.01.011.

Grafana Labs. Grafana. `https://github.com/grafana/grafana`, 2025. Accessed: 2025-01-15.

P. K. F. Grieder. *Cosmic Rays at Earth: Researcher's Reference Manual and Data Book*. Elsevier, Amsterdam, Netherlands, 2001. ISBN 978-0-444-50710-5.

B. Hariharan, M. Chakraborty, S.R. Dugad, S.K. Gupta, Y. Hayashi, P. Jagadeesan, A. Jain, S. Kawakami, H. Kojima, S. Mahapatra, P.K. Mohanty, Y. Muraki, P.K. Nayak, T. Nonaka, A. Oshima, D. Pattanaik, M. Rameez, K. Ramesh, L.V. Reddy, S. Shibata, and M. Zuberi. Probing solar storms with GRAPES-3 scintillator detectors. *Journal of Atmospheric and Solar-Terrestrial Physics*, 243:106005, 2023. ISSN 1364-6826. doi: https://doi.org/10.1016/j.jastp.2023.106005. URL `https://www.sciencedirect.com/science/article/pii/S1364682623000032`.

K. Kampert and A. Watson. Extensive air showers and ultra high-energy cosmic rays: a historical review. *The European Physical Journal H*, 37(3):359–412, 2012.

Gerald R. Lynch and Orin I. Dahl. Approximations to multiple Coulomb scattering. *Nuclear Instruments and Methods in Physics Research Section B: Beam Interactions with Materials and Atoms*, 58(1):6–10, 1991. ISSN 0168-583X. doi: https://doi.org/10.1016/0168-583X(91)95671-Y.

A. Maghrabi and M. Almutairi. The influence of several atmospheric variables on cosmic ray muons observed by KACST detector. *Advances in Space Research*, 62(11):3267–3277, 2018. ISSN 0273-1177. doi: 10.1016/j.asr.2018.08.021.

R. R. S. Mendonça, C. Wang, C. R. Braga, E. Echer, A. Dal Lago, J. E. R. Costa, K. Munakata, H. Li, Z. Liu, J.-P. Raulin, T. Kuwabara, M. Kozai, C. Kato, M. Rockenbach, N. J. Schuch, H. K. Al Jassar, M. M. Sharma, M. Tokumaru, M. L. Duldig, J. E. Humble, P. Evenson, and I. Sabbah. Analysis of Cosmic Rays' Atmospheric Effects and Their Relationships to Cutoff Rigidity and Zenith Angle Using Global Muon Detector Network Data. *Journal of Geophysical Research: Space Physics*, 124(12): 9791–9813, 2019. doi: https://doi.org/10.1029/2019JA026651.

A. Mishev and S. Poluianov. About the altitude profile of the atmospheric cut-off of cosmic rays: new revised assessment. *Solar Physics*, 296(8):129, 2021. doi: 10.1007/s11207-021-01875-5.

Arfa Mubashir, Ashwin Ashok, Megan Connors, Xiaochun He, H.A. Tharindu G. Hettiarachchi, Petrus Martens, Enosh H. Mudiyanselage, Unil A.G. Perera, Ernesto Potdevin, Viacheslav M. Sadykov, Murad Sarsour, Mihailo Savić, and Nikola Veselinović. Time lag analysis of the space weather effects on muon and neutron flux at different geomagnetic cutoff rigidities. *Advances in Space Research*, 2025. ISSN 0273-1177. doi: https://doi.org/10.1016/j.asr.2025.04.032. URL `https://www.sciencedirect.com/science/article/pii/S0273117725003680`.

K. Munakata, M. Kozai, C. Kato, Y. Hayashi, R. Kataoka, A. Kadokura, M. Tokumaru, R. R. S. Mendonça, E. Echer, A. Dal Lago, M. Rockenbach, N. J. Schuch, J. V. Bageston, C. R. Braga, H. K. Al Jassar, M. M. Sharma, M. L. Duldig, J. E. Humble, I. Sabbah, P. Evenson, P.-S. Mangeard, T. Kuwabara, D. Ruffolo, A. Sáiz, W. Mitthumsiri, W. Nuntiyakul, and J. Kóta. Large-amplitude Bidirectional Anisotropy of Cosmic-Ray Intensity Observed with Worldwide Networks of Ground-based Neutron Monitors and Muon Detectors in 2021 November. *The Astrophysical Journal*, 938(1):30, oct 2022. doi: 10.3847/1538-4357/ac91c5.

A. Neiser, J. Adamczewski-Musch, M. Hoek, W. Koenig, G. Korcyl, S. Linev, L. Maier, J. Michel, M. Palka, M. Penschuck, M. Traxler, C. Uğur, and A. Zink. TRB3: a 264 channel high precision TDC platform and its applications. *Journal of Instrumentation*, 8(12):C12043–C12043, 2013. doi: 10.1088/1748-0221/8/12/c12043.

D. Reyna. A simple parameterization of the cosmic-ray muon momentum spectra at the surface as a function of zenith angle, 2006. URL `https://arxiv.org/abs/hep-ph/0604145`.

M. Rockenbach, A. Dal Lago, N. J. Schuch, K. Munakata, T. Kuwabara, A. G. Oliveira, E. Echer, C. R. Braga, R. R. S. Mendonça, C. Kato, M. Kozai, M. Tokumaru, J. W. Bieber, P. Evenson, M. L. Duldig, J. E. Humble, H. K. Al Jassar, M. M. Sharma, and I. Sabbah. Global Muon Detector Network Used for Space Weather Applications. *Space Science Reviews*, 182:1–18, 2014. doi: 10.1007/s11214-014-0048-4.

B. Rossi. *Cosmic Rays*. McGraw-Hill, New York, 1964. ISBN 978-0-07-053890-0.

João Saraiva and Alberto Blanco. New readout scheme for large area timing & position RPCs. *Nuclear Instruments and Methods in Physics Research Section A: Accelerators, Spectrometers, Detectors and Associated Equipment*, 1068:169803, 2024. ISSN 0168-9002. doi: https://doi.org/10.1016/j.nima.2024.169803. URL `https://www.sciencedirect.com/science/article/pii/S0168900224007290`.

R. Sehgal, M. Sengupta Mitra, Tushar Roy, S.T. Sehgal, L.M. Pant, and B.K. Nayak. Voxelization-based PoCA point cloud filtration algorithm for image reconstruction for Muon Tomography. *Journal of Instrumentation*, 15:P09012, September 2020. doi: 10.1088/1748-0221/15/09/P09012.

Iván Sidelnik and Hernán Asorey. LAGO: The Latin American giant observatory. *Nuclear Instruments and Methods in Physics Research Section A: Accelerators, Spectrometers, Detectors and Associated Equipment*, 876:173–175, 2017. ISSN 0168-9002. doi: https://doi.org/10.1016/j.nima.2017.02.069. URL `https://www.sciencedirect.com/science/article/pii/S0168900217302656`. The 9th international workshop on Ring Imaging Cherenkov Detectors (RICH2016).

C. Soneira-Landín, A. Blanco, L.M. Fraile, Juan A. Garzón, G. Kornakov, L. Lopes, V.M. Nouvilas, and J.M. Udías. miniTRASGO: A compact RPC tracker for cosmic ray studies. *Nuclear Instruments and Methods in Physics Research Section A: Accelerators, Spectrometers, Detectors and Associated Equipment*, 1077:170511, 2025. ISSN 0168-9002. doi: https://doi.org/10.1016/j.nima.2025.170511. URL `https://www.sciencedirect.com/science/article/pii/S0168900225003122`.

C. T Steigies, M. Thomann, O. Rother, R. Wimmer-Schweingruber, and B. Heber. Real-time database for high resolution neutron monitor measurements. In *Proc. 30th ICRC*, volume 1, pages 303–306, 2008.

The Pierre Auger Collaboration. The Pierre Auger Cosmic Ray Observatory. *Nuclear Instruments and Methods in Physics Research Section A: Accelerators, Spectrometers, Detectors and Associated Equipment*, 798:172–213, 2015. ISSN 0168-9002. doi: https://doi.org/10.1016/j.nima.2015.06.058.

The Pierre Auger Collaboration. Scaler Rates from the Pierre Auger Observatory: A New Proxy of Solar Activity. *The Astrophysical Journal*, 987(1):41, jun 2025. doi: 10.3847/1538-4357/adccc3. URL `https://dx.doi.org/10.3847/1538-4357/adccc3`.

J. L. Uretsky. Penetration of cosmic ray muons into the Earth. *Nuclear Instruments and Methods in Physics Research Section A: Accelerators, Spectrometers, Detectors and Associated Equipment*, 399(2): 285–300, 1997. ISSN 0168-9002. doi: 10.1016/S0168-9002(97)00996-0.

D. F. Webb and T. A. Howard. Coronal Mass Ejections: Observations. *Living Reviews in Solar Physics*, 9:3, 2012. doi: 10.12942/lrsp-2012-3.

M. Xarepe, T. Aumann, A. Blanco, A. Corsi, D. Galaviz, H.T. Johansson, S. Linev, B. Löher, L. Lopes, J. Michel, V. Panin, D. Rossi, J. Saraiva, H. Törnqvist, and M. Traxler. Resistive plate chambers for precise measurement of high-momentum protons in short range correlations at R3B. *Nuclear Instruments and Methods in Physics Research Section A: Accelerators, Spectrometers, Detectors and Associated Equipment*, 1055:168445, 2023. ISSN 0168-9002. doi: 10.1016/j.nima.2023.168445.

E. Cerron Zeballos, I. Crotty, D. Hatzifotiadou, J. Lamas Valverde, S. Neupane, M.C.S. Williams, and A. Zichichi. A new type of resistive plate chamber: The multigap RPC. *Nuclear Instruments and Methods in Physics Research Section A: Accelerators, Spectrometers, Detectors and Associated Equipment*, 374(1):132–135, 1996. ISSN 0168-9002. doi: 10.1016/0168-9002(96)00158-1.